Infrared photodetection in graphene-based heterostructures: bolometric and thermoelectric effects at the tunneling barrier

Check for updates

Dmitry A. Mylnikov [1,9] ✉, Mikhail A. Kashchenko[1,2,9], Kirill N. Kapralov[1], Davit A. Ghazaryan [3,4], Evgenii E. Vdovin [5], Sergey V. Morozov[5], Kostya S. Novoselov [6], Denis A. Bandurin [7] ✉, Alexander I. Chernov [1,8] & Dmitry A. Svintsov [1] ✉

Graphene/hBN/graphene tunnel devices offer promise as sensitive mid-infrared photodetectors but the microscopic origin underlying the photoresponse in them remains elusive. In this work, we investigated the photocurrent generation in graphene/hBN/graphene tunnel structures with localized defect states under mid-IR illumination. We demonstrate that the photocurrent in these devices is proportional to the second derivative of the tunnel current with respect to the bias voltage, peaking during tunneling through the hBN impurity level. We revealed that the origin of the photocurrent generation lies in the change of the tunneling probability upon radiation-induced electron heating in graphene layers, in agreement with the theoretical model that we developed. Finally, we show that at a finite bias voltage, the photocurrent is proportional to either of the graphene layers heating under the illumination, while at zero bias, it is proportional to the heating difference. Thus, the photocurrent in such devices can be used for accurate measurements of the electronic temperature, providing a convenient alternative to Johnson noise thermometry.

Mid-infrared (mid-IR) photodetectors hold immense importance across diverse fields. Capturing and visualizing thermal radiation, they enable the study of celestial objects and their evolution[1,2], diagnostics and therapeutics through non-invasive imaging[3], nondestructive testing of components and detecting defects[4]. Mid-IR light carries information about molecular vibrations, providing valuable information about the chemical composition of materials for monitoring environmental pollutants[5].

Tunneling devices based on van der Waals heterostructures are attractive for infrared detection due to the presence of strong phonon-polariton absorption lines in many layered dielectrics[6–9], the most prominent example being the hyperbolic modes of hexagonal boron nitride (hBN)[10–12]. The intrinsic response time of tunneling detectors should be very short and limited only by vertical transport between few-nanometer-thick barriers[13,14]. As the tunneling probability is exponentially sensitive to the electron energy and barrier height, the tunnel-type photodetectors may have additional photocurrent gain mechanisms. They can be associated either with carrier heating or light-induced charge accumulation in the layers. The latter effect is especially pronounced in multilayer structures, such as those used in quantum well infrared photodetectors[15–17]. Strong non-linearity of the tunneling current–voltage characteristic should give rise to a pronounced radiation rectification, at least at 'classical' electromagnetic frequencies, when photon energy is below the barrier

[1]Center for Photonics and 2D Materials, Moscow Institute of Physics and Technology, Dolgoprudny 141700, Russia. [2]Programmable Functional Materials Lab, Center for Neurophysics and Neuromorphic Technologies, Moscow 127495, Russia. [3]Laboratory of Advanced Functional Materials, Yerevan State University, Yerevan 0025, Armenia. [4]Moscow Center for Advanced Studies, Kulakova str. 20, Moscow 123592, Russia. [5]Institute of Microelectronics Technology RAS, Chernogolovka 142432, Russia. [6]Institute for Functional Intelligent Materials, National University of Singapore, Singapore 117575, Singapore. [7]Department of Materials Science and Engineering, National University of Singapore, Singapore 117575, Singapore. [8]Russian Quantum Center, Skolkovo Innovation City, Moscow 121205, Russia. [9]These authors contributed equally: Dmitry A. Mylnikov, Mikhail A. Kashchenko. ✉e-mail: mylnikov.da@yandex.ru; bandurin.d@gmail.com; svintcov.da@yandex.ru

height[18,19]. At 'quantum' frequencies, a more adequate picture of photocurrent is the photon-assisted tunneling[20]. The photon-aided tunneling should benefit from singularities in the joint density of states between tunnel-coupled layers. Such a situation is realized in superlattice-based photodetectors[21,22] and quantum cascade lasers[23] and is further anticipated for tunnel-coupled graphene layers[24,25].

A variety of light-induced physical effects in tunnel-coupled 2D layers makes it challenging to reveal the dominant photodetection mechanism in such structures. The experimental studies of such structures were concentrated on the visible range, where both heating-induced photocurrents[26,27] and direct photon-aided tunneling were detected[28]. A reverse process of tunneling accompanied by visible light emission was also observed in coupled graphene layers[29]. The measurements of van der Waals tunneling photodetectors at lower electromagnetic frequencies are scarce. In the THz range, the measured photocurrents were speculated to originate from photon-aided tunneling[30], yet no experimental proofs of this scenario were provided. As a result, the mechanism of photocurrent generation in graphene-based vertical tunnel structures in the infrared range remains unresolved.

In this work, we report on the photocurrent measurements of graphene/hBN/graphene tunnel structure under IR illumination with a photon energy of 144–207 meV. The graphene layers in our structures are twisted by a large angle $\gtrsim 5°$ [31,32]. In such a situation, the direct current can be dominated by electron resonant hopping via impurity levels inside the hBN barrier[33,34], where the I_b–V_b-characteristic becomes ladder-type with sharp slopes. We find that the photocurrent I_{ph} is proportional to the $d^2 I_b/dV_b^2$ and is maximum under the condition of tunneling through the impurity level in hBN. At a non-zero bias, the photocurrent appears proportional to the derivative of the DC tunnel current with respect to the base cryostat temperature dI_b/dT. The proportionality between these three quantities (the photocurrent, the curvature of I_b–V_b-characteristic, and the temperature derivative of DC current) is accurately reproduced by a theoretical model where the incident radiation causes electron heating in coupled graphene layers. At finite bias, the origin of photocurrent can be termed as bolometric effect across the tunnel junction. At zero bias, the photocurrent emerges only upon the asymmetric heating of electrons in the two layers. The phenomenon is analogous to the photo-thermoelectric effect, albeit it is developed across the tunnel barrier. As the main reason for tunneling photocurrent lies in the radiation-induced electron heating, it becomes possible to perform the inverse reconstruction of electron temperature from the measured photocurrent. Such a technique can become a simple alternative to the Johnson noise thermometry[35], especially at cryogenic temperatures[36–39].

Results

Electrical characterization of tunneling infrared detector

Our tunnel IR detector was fabricated using dry transfer technique[40] (see the "Methods" section for details). The structure consists of two flakes of single-layer graphene (SLG) separated by approximately three layers of hBN (thickness ~1 nm). The structure is located on an hBN/graphite stack, the latter serving as a back gate. The intersection area of the top and bottom graphene is ~2.3 μm², which determines the area of the tunnel junction. A scheme of the stack and measurement configuration are presented in Fig. 1a. A photograph of the heterostructure with marked contacts used for measurements is shown in Fig. 1b. During measurements, the device was held in a cryostat at a base temperature of 7 K, unless otherwise is indicated.

Electrical measurements of the tunnel structure (Fig. 1c) confirm the rotational misalignment of graphene layers and the presence of resonant states in the dielectric. First of all, no traces of negative differential resistance are observed in the I_b–V_b-curves, which implies strong misorientation of graphene crystal structures. Second, the current-voltage characteristic has pronounced "steps", which indicate the opening of new tunneling channels with an increase in the bias voltage. The detailed mapping of differential conductance dI_b/dV_b vs. gate and bias voltages shown in Fig. 1d confirms that these tunneling paths are associated with a resonant passage of electrons through the impurity levels. We identify four characteristic spike lines in the differential conductance map, marked as $i1_t$, $i2_t$, $i1_b$, and $i2_b$. The spike positions depend on both bias and gate voltage, the latter controlling the carrier density. This excludes the phonon-assisted origin of conduction. Instead, each spike can be attributed to the alignment of the Fermi level in either graphene layer $\mu_{t,b}$ with the level of impurity inside the band gap of boron nitride (Fig. 1e). More precisely, the resonant condition can be formulated as

$$\mu_{t,b}(V_b, V_{gate}) = E_{i,n} + eF(V_b, V_{gate})x_{i,n}, \qquad (1)$$

where $E_{i,n}$ is the energy level of nth impurity in the absence of bias, the second term represents the bias-induced shift of impurity level, F is the electric field in the hBN barrier, and $x_{i,n}$ is the position of the nth impurity.

We managed to reproduce the experimentally measured positions of conduction spikes with the model (1) assuming two resonant levels within the barrier. The fitting procedure yields the defect levels $E_{i1} = 100$ meV and $E_{i2} = -70$ meV reckoned from the Dirac points of unbiased layers. Further fitting enables the determination of impurity positions: impurity #1 is located in the middle of the barrier, while impurity #2 is between the second and third hBN layers, counted from the bottom graphene. We also observe

Figure 1

Fig. 1 | Tunneling detector scheme and electrical characterization. a The stack scheme of the tunneling detector. **b** Optical photograph of the sample with false-color images of the top, bottom graphene, and barrier hBN superimposed on it. Contacts to the top and bottom graphene used in measurements are designated by the letters "T" and "B" accordingly. AFM scan of barrier hBN edge is shown in the inset. There is a cutout in the stack made to avoid possible shorting of the top and bottom graphene. Scale bar is 10 μm. **c** I_b−V_b device characteristics at different gate voltages, showing ladder-type behavior. **d** Map of differential conductance as a function of bias and gate voltages at 7 K. The curves of maximum conductance are marked with $i1_t$, $i2_t$, $i1_b$, $i2_b$, and arrows of minimum conductance—cnp_t, cnp_b and blue dotted lines. The black dotted lines correspond to the theory. **e** Illustration of the tunneling process when the 1st impurity is aligned with the bottom graphene Fermi level, which corresponds to the $i1_b$-curve on (**d**). **f** Same illustration, but the impurity is aligned with the bottom graphene CNP (cnp_b-curve on (**d**)).
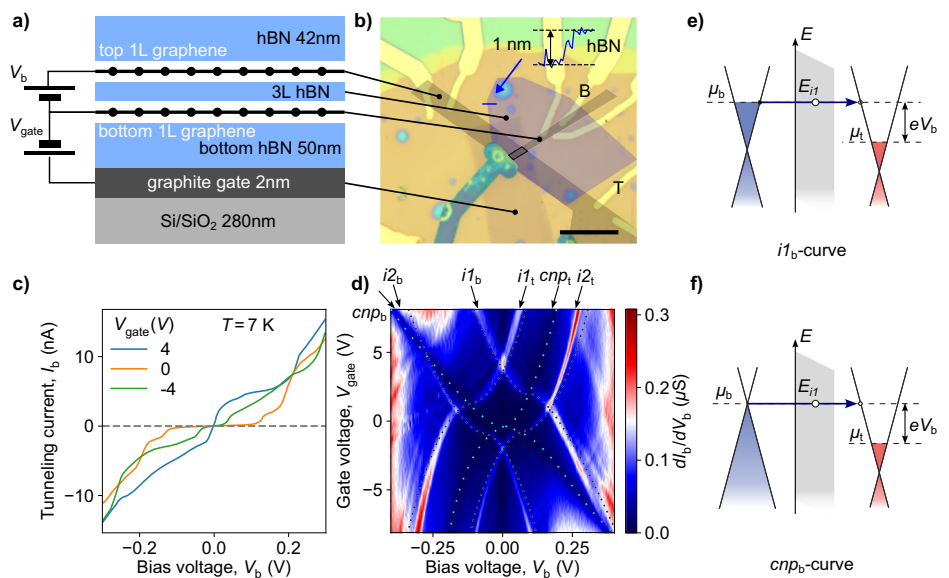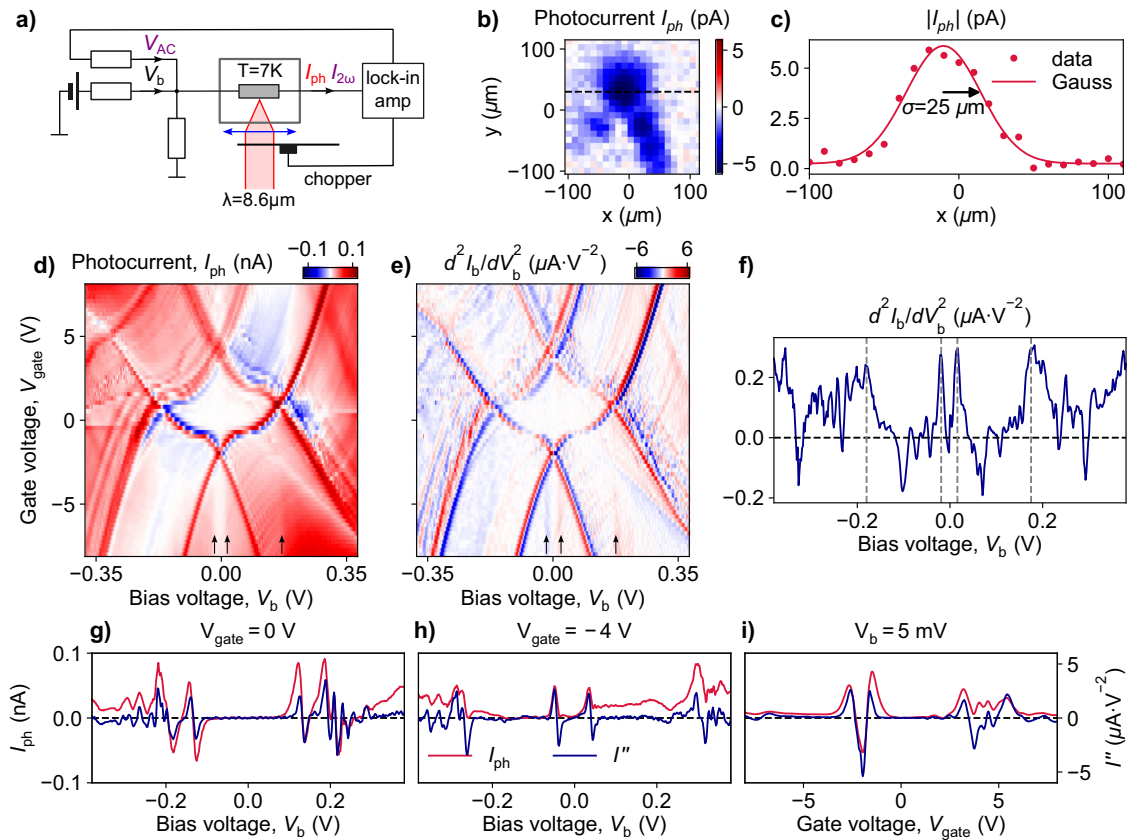
Fig. 2 | Photocurrent measurements under $\lambda = 8.6$ μm illumination at $T = 7$ K. **a** Scheme of the photocurrent and d^2I_b/dV_b^2 measurements. **b** Spatial photocurrent map. Deviation of the spot from the symmetrical Gaussian shape is aberration due to a slightly oblique incidence of light on the lens but not the sample features. **c** Slice of the map at $y = 30$ μm and spot size extracted by fitting to Gaussian distribution. **d** Photocurrent as a function of bias and gate voltages. **e** Second derivative of $I_b(V_b)$

as a function of bias and gate voltages. It's clearly seen how the photocurrent repeats all d^2I_b/dV_b^2 features in details. **f** d^2I_b/dV_b^2 averaged over all gate voltages. **g–i** Slices of maps (**d**) and (**e**) at two different gate voltages: **g** $V_{gate} = 0$ V, **h** $V_{gate} = -4$ V and **i** at small bias $V_b = 5$ mV. Features at the energies of the phonon modes are marked by arrows on (**d**, **e**) and by vertical dashed lines on (**f**).

many other fainter resonant lines (curves near $i1$ and parallel to it) that emerge from other impurities, probably having a smaller overlap with the tunnel barrier.

Another prominent feature of the conduction map is the area with nearly zero differential conductivity. It forms two dark blue curves in Fig. 1d, labeled cnp_t and cnp_b. It corresponds to the neutrality point of either graphene layer and, hence, to zero tunneling density of states (DOS) (Fig. 1f). Both cnp-curves cross at nearly zero gate and bias voltages, which implies the absence of initial doping in both graphene layers. It can be noted that tunneling through impurity does not occur on these curves; lines $i1$ and $i2$ are interrupted.

Photocurrent under mid-infrared illumination
We proceed to the characterization of the tunneling structure in the photodetector mode. The device is illuminated with mid-infrared radiation $\lambda = 8.6$ μm fed from a quantum cascade laser with output power $P \approx 7.2$ mW. The photocurrent is measured using a lock-in amplifier (see Fig. 2a and the "Methods" section for details). The photocurrent map recorded by moving the laser beam across the device represents a single bright spot (Fig. 2b, c). This excludes the role of contact effects in the photocurrent generation process and shows that the tunnel structure itself acts as a photocurrent generator.

Figure 2 d shows the gate- and bias-resolved map of the photocurrent. First, the correlation of the photocurrent extrema with the position of the impurities on the differential conductance map is striking. The photocurrent extrema very closely follows the curves $i1$ and $i2$ of the differential conductance map, i.e. are observed when the Fermi levels of impurities and

graphene layers are aligned. The next interesting feature is that when V_b changes, and the impurity level passes through the Fermi level of one of the graphene layers, the photocurrent has two extrema of opposite signs, which are observed at $|V_b| < 0.25$ V, $|V_{gate}| < 3$ V. At large values of the bias and gate, these features persist, yet the photocurrent acquires a positive 'background' growing with the absolute value of bias.

The correlation between optoelectronic and electrical properties becomes even more apparent upon comparison of the photocurrent map with the d^2I_b/dV_b^2 map shown in Fig. 2e. They match in the smallest details. The photocurrent extrema follows the d^2I_b/dV_b^2 extrema for all values of the bias and gate, repeating the position dependencies on V_{gate} and V_b not only for the two main impurities but also for all others. For example, with negative gate and offset values, there are several impurities nearby. The photocurrent is amplified at each. At small values of V_b and V_{gate} (namely, at $|V_b| < 0.25$ V, $|V_{gate}| < 3$ V) there is a direct proportionality between the photocurrent and d^2I_b/dV_b^2 clearly visible on the map slices in Fig. 2g–i. At larger gate and bias voltages, the presence of the background in photocurrent weakens this similarity, as indicated in Fig. 2h. In this regime, d^2I_b/dV_b^2 has a strong sign-changing feature upon crossing the impurity level. The photocurrent does not change sign at these bias voltages, yet it demonstrates a spike at these points.

In addition, at $V_b \approx \pm 18$–20 mV and $V_b \approx 175$–200 mV the photocurrent map shows features that do not depend on V_{gate}, expressed in a sudden increase in I_{ph} with increasing V_b. The latter energy is greater than the energy of the incident photon (144 meV) and coincides with the energy of the optical phonon modes of graphene. These features are also visible on the d^2I_b/dV_b^2 map as local extrema. They are marked with small black

Fig. 3 | Illustration and theory of the photocurrent generation. a and **b** Illustration of the thermal mechanism of the photocurrent generation when the top graphene layer is biased slightly (**a**) below or (**b**) above the impurity level (which corresponds to $i1_b$, $i2_b$-curves on Fig. 1d). **c** Illustration of the photocurrent generation at zero bias at 2 gate voltages near impurity alignment. **d** Theoretically calculated photocurrent and **e** $d^2 I_b / dV_b^2$ map as a function of gate and bias voltages, well reproducing experimental results. **f** and **g** Slices of maps **d** and **e** at three different bias voltages: **f** $V_b = 0.25$ V; **g** $V_b = 5$ mV, along dashed line on (**d**); **h** $V_b = 0$. The red dashed and dotted lines on **g**, **h** demonstrate the contribution of the top and bottom layers, respectively, to the total photocurrent. The heating of the layers is assumed to be slightly different, $\delta T_t = 1.2 \delta T_b$, which gives a non-zero photocurrent at $V_b = 0$.
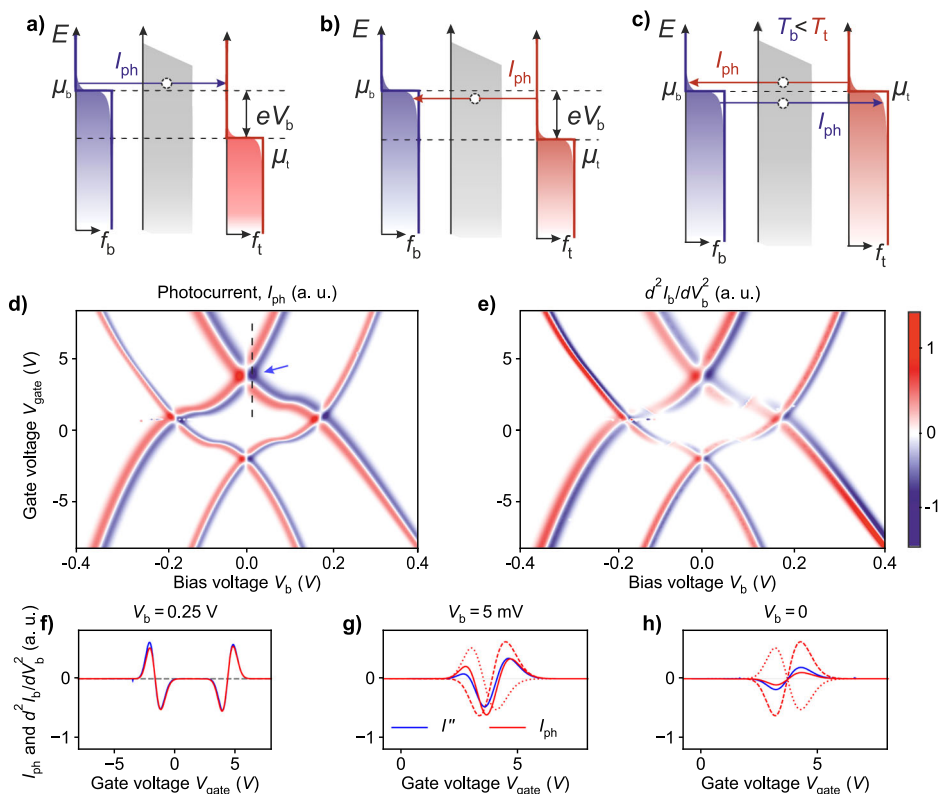
arrows in Fig. 2d, e. The resonances are visible even better if one average the $d^2 I_b / dV_b^2$ dependences over all values of V_{gate} (Fig. 2f). This coincides with previously observed phonon modes of graphene obtained from transport measurements[33,41]. Moreover, while low-energy phonon modes have already been observed as phonon-assisted photocurrent under illumination with visible light, high-energy optical modes have been demonstrated. While in ref. 41 other phonon modes were also observed; they are less pronounced compared to the ones mentioned above and, for this reason, are not visible in our device.

All the key features of the dependencies of the photocurrent on the gate and bias, namely the proportionality of the photocurrent to the 2nd derivative of $I_b(V_b)$, the presence of two extrema of the opposite sign when the levels of graphene and impurity are aligned, were repeated in the measurements of the device #2 (Supplementary Note 2). The device was a graphene/hBN/graphene stack encapsulated in protective hBN layers with the same hBN barrier thickness of 1 nm. The stack was different in that it was made of multilayer graphene (2L on top and 3L on the bottom), had a large tunnel junction area and a silicon gate, and was illuminated at a different wavelength of 6.0 μm.

Origins of photocurrent: bolometric and thermoelectric effects at the tunnel barrier

The two competing mechanisms contributing to the photocurrent in tunnel-coupled low-dimensional systems are photon-assisted tunneling and the tunneling of hot carriers. The direct rectification by nonlinearity of the tunneling I_b–V_b-characteristic should be considered as a low-frequency limit of the photon-aided tunneling and does not require a separate consideration. Were the photon-aided tunneling a dominant light detection mechanism, the photocurrent should peak when the Fermi level $\mu_{t,b}$ plus the photon energy $\hbar\omega$ reaches the level of impurity E_i[42–45]. Such energy constraint corresponds to the onset of tunneling by photoexcited carriers along the resonant levels. The photocurrent map for this detection mechanism should possess extrema curves parallel to the impurity lines $i1_t$, $i2_t$ and shifted by $\hbar\omega = 144$ meV on the bias scale.

We observe no peculiarities of $I_{ph}(V_b, V_{gate})$ at these energies and, therefore, exclude photon-assisted tunneling from relevant photodetection mechanisms.

An alternative to the photon-assisted tunneling realized in the case of fast inter-carrier energy exchange is the tunneling of electrons heated up by absorbed radiation. The light-induced change in electron temperature leads to the broadening of their Fermi distributions and, hence, to the change in average tunneling probability. Further physics depends essentially on whether the layers are biased or not and on the relative position of Fermi levels and impurity levels.

For biased structures, the photocurrent represents the change in total tunneling current induced by carrier heating. If the Fermi level of a particular graphene layer is biased slightly below the impurity level *in the dark*, the light-induced heating would push the electrons toward the resonant level. This would increase the total current and lead to a positive spike in the photocurrent (Fig. 3a). If the same layer is biased slightly above the impurity level *in the dark*, the light-induced heating would deplete the Fermi distribution in the vicinity of resonant energy. In such a situation, the negative spike in the photocurrent would be observed (Fig. 3b). Such a double-spike structure of photocurrent is indeed observed each time the Fermi level $\mu_{t,b}$ crosses the impurity level at not very large bias voltages (Fig. 2g). This fact can already be considered as a proof of hot-carrier origin of the photocurrent.

At near-zero bias, the Fermi levels of both graphene layers are very close. When the impurity level is aligned with them, the two effects described above are superimposed on each other, resulting in a picture with three spikes, which we observed at $V_b = 5$ mV (Fig. 2i).

At zero bias, the origin of photocurrent is distinct and can be termed as Seebeck effect across the tunnel barrier. Heating of both top and bottom electronic subsystems by the same amount cannot result in any current due to their partial thermal equilibrium. However, asymmetric heating of electrons in the layers would result in an imbalance between tunneling currents, measured as photocurrent. The photocurrent would be, therefore, proportional to the temperature difference between the layers, $I_{ph} \propto T_t - T_b$.

Fig. 4 | Estimation of the temperature of the electron gas heated by radiation from dI_b/dT and photocurrent measurements. a dI_b/dT and photo-current as a function of bias voltage measured at $V_{gate} = 0$, **b** as a function of gate voltage at small bias $V_b = 5$ mV. Electron temperature rise is estimated to be about 8 K. **c** and **d** Theoretically calculated photo-current and dI_b/dT for **c** $V_{gate} = 0$ and **d** $V_b = 5$ mV for $\delta T_t = 1.2 \delta T_b$. **e** Photocurrent dependence on V_b at elevated temperatures.
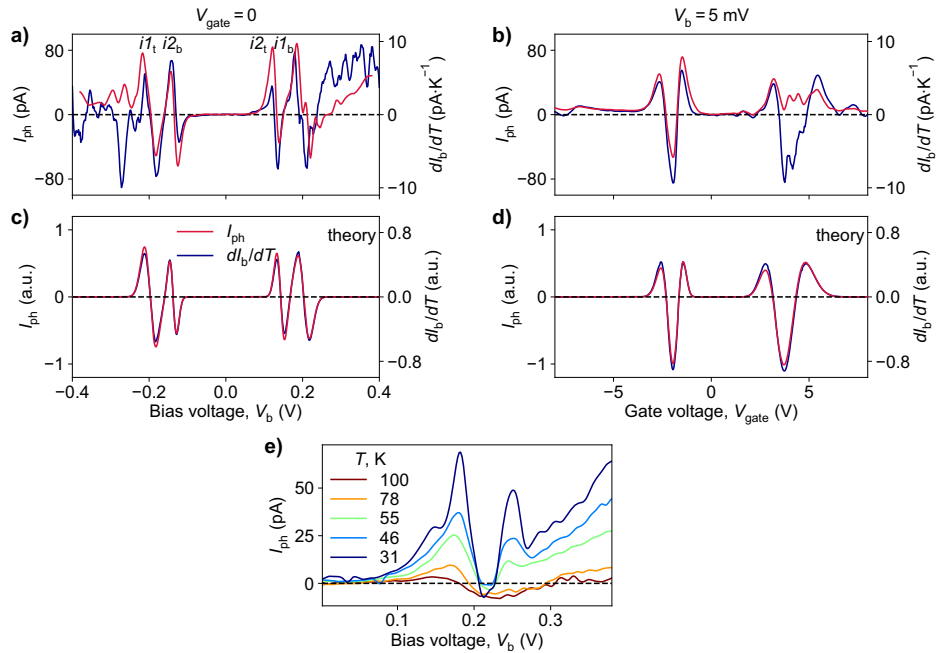
Further proofs of the thermal origin of the photocurrent can be obtained by direct calculation of temperature-dependent current–voltage characteristics $I_b(T_t, T_b)$. We have obtained the latter with the Bardeen transfer Hamiltonian approach

$$I_b(T_t, T_b) = \frac{e}{\hbar} \int_{-\infty}^{\infty} dE \left[f_t(E) - f_b(E) \right] \mathcal{D}(E), \qquad (2)$$

where $f_{t,b} = [1 + \exp((E - \mu_{t,b})/k_B T_{t,b})]^{-1}$ are the Fermi distribution functions in top and bottom layers with generally different temperatures (T_t and T_b) and Fermi levels. The function $\mathcal{D}(E)$ is the energy-dependent tunneling probability possessing sharp resonances at impurity levels $E = E_{i,n}$ (see[34] and the Supplementary Note 3 for explicit form). The model (2) is suitable both for calculations of DC source-drain current (with all its derivatives) and the photocurrent. For DC current, one sets the temperatures of both layers to the base cryostat temperature $T_t = T_b = T_0$. Evaluating the photocurrent, one sets $T_{t,b} = T_0 + \delta T_{t,b}$, where $\delta T_{t,b}$ are the light-induced overheating of top and bottom layer. In explicit form

$$I_{ph} = I(T_0 + \delta T_t, T_0 + \delta T_b) - I(T_0). \qquad (3)$$

The results of photocurrent calculations are presented in Fig. 3d–h and fully confirm the above intuitive picture on light-induced heating effects. Under finite bias V_b, the theoretically predicted photocurrent indeed possesses upward and downward spikes at both sides of impurity levels. Moreover, the theory reproduces the observed proportionality between photocurrent and $d^2 I_b/dV_b^2$, which can be derived analytically in a fashion similar to the derivation of Wiedemann-Franz law (see Supplementary Note 3 for details).

At a bias close to zero, the photocurrent is a superposition of the photocurrent profiles from two graphene layers. At a bias of exactly zero, their sum gives the dependence of the photocurrent on the gate in the form of two spikes of opposite signs, the amplitudes of which are proportional to the temperature difference of the graphene layers $I_{ph} \propto \delta T_t - \delta T_b$ (Fig. 3h).

However, applying even a small bias $V_b = 5$ mV spoils this ideal picture. The photocurrent profiles from the two layers are summed up into a pattern with three spikes: two upward (downward) spikes and a single downward

(upward). A strong central spike mostly corresponds to the sum of the co-directional photocurrents from both graphene layers and represents the average heating of the graphene layers. While the two side spikes represent the sum of the opposing photocurrents from the two layers and contain information about the temperature difference between the layers (Fig. 3g). This is exactly what we see in the experiment at $V_b \approx 0$ mV (Fig. 2i). The accuracy of setting and measuring the voltage did not allow us to clearly catch the case of zero bias (Supplementary Fig. 3).

Once the origin of photocurrent is thermal, its functional dependence $I_{ph}(V_b, V_{gate})$ should be similar to that of temperature conductance coefficient dI_b/dT_0. Independent measurements of photocurrent and tunnel current $I_b(T_0)$ with variable base cryostat temperature confirm this idea, as shown in Fig. 4a, b.

More precisely, in a linear approximation of Eq. (3) on temperature, the photocurrent is given by

$$I_{ph} = \frac{dI_b}{dT_t} \delta T_t + \frac{dI_b}{dT_b} \delta T_b. \qquad (4)$$

When $eV_b \gg k_B T_0 \approx 0.7$ meV and away from the $i1_t$, $i1_b$, $i2_t$, $i2_b$ lines crossing areas determined by the energy width of the impurity levels (≈ 4 meV), photocurrent depends only on $dI_b/dT\delta T$ of one of the graphene layers, which Fermi level is aligned with the impurity level. The Fermi level of the other graphene layer is far away and does not significantly contribute to the photocurrent. It becomes possible to calculate the increase in the electron temperature of each layer by dividing the measured photocurrent value by dI_b/dT at curves $i1_t, i2_t$ for the top layer and $i1_b, i2_b$ for the bottom.

We calculated the derivative of the current with respect to temperature as $dI_b/dT = (I_b(T_2) - I_b(T_1))/(T_2 - T_1)$, where T_1, T_2 are 10 and 20 K for Fig. 4a, and 7 and 20 K for Fig. 4b. Comparing its profile with the photo-current measured at 7 K at the positions of spikes $i1_t, i2_t, i1_b, i2_b$, we estimate the average heating of electrons in both graphene layers at our incident light power 7.2 mW to be $\delta T \approx 8$ K. The spread of the top and bottom layer heating values does not allow us to estimate their difference.

In the unbiased case, we did not observe ideal photocurrent profiles with two spikes, only a pattern corresponding to a near-zero bias. This still allows us to evaluate the difference in heating of the graphene layers. Fitting calculated $I_{ph}(V_{gate})$ curves at $V_b = 5$ mV to the experimental data, we estimate the temperature difference between the layers to be $\lesssim 1.5$ K.

As the temperature increases, the Fermi distribution blurs, which, according to the theory, leads to a decrease in dI_b/dT inversely proportional to temperature, and hence to a decreasing in the photocurrent. In Fig. 4e the photocurrent dependence on V_b is presented at different temperatures from 31 to 100 K, demonstrating a decline with increasing the temperature, as expected.

Discussion

In summary, we have elucidated the mechanism of photocurrent generation in graphene/hBN/graphene tunnel structures with localized defect states in a barrier upon mid-infrared illumination. The photocurrent appears upon electron heating, resulting either in a Seebeck-type effect at zero bias or in a bolometric effect at finite bias. Both effects differ from their classical counterparts observed upon longitudinal Ohmic transport, as here they develop across the tunneling barrier. Both effects are maximized at the gate and bias voltages corresponding to the $I(V)$-curve steps. At these steps, the Fermi level of either graphene layer is aligned with a resonant-tunneling defect state and even tiny changes in electron temperature result in strong variations of the energy-averaged electron tunneling probability.

We have developed a theoretical model of such photo-thermal tunneling current and reproduced the experimental data in detail at all bias and gate voltages. At cryogenic temperatures $T \sim 9$ K corresponding to the actual experiment, the photothermoelectric effect across the barrier is observed only at very low bias voltages $V_b \lesssim kT/e \sim 1$ mV and surpasses the bolometric effect otherwise. At nearly room temperature, the thermoelectric effect is observed in a much broader range of biases.

Absence of a direct photon-assisted tunneling component in the observed photocurrent may lie in the fast thermalization of photoexcited electrons, as compared to their tunneling exchange between layers. The scattering time of electron above the Fermi surface scales quadratically with its elevation[46], thus $\tau_{th} \approx 4\pi\varepsilon_F/\hbar\omega^2$. The corresponding thermalization time at a realistic Fermi energy at $\varepsilon_F = 200$ meV estimates to $\tau_{th} \approx 80$ fs. The tunneling time can be estimated $\tau_{tun} = (\hbar/E_{bar})e^{2\kappa d_{bar}}$, where $E_{bar} \approx 1.5$ eV is the barrier height at the graphene/hBN interface and $\kappa \approx 6$ nm^{-1} is the electron wave function decay rate[47]. For barrier thickness $d \approx 1$ nm, the tunneling time $\tau_{tun} \approx 40$ ps appears three orders of magnitude longer than the thermalization time. At lower excitation frequencies $\omega/2\pi \lesssim 1$ THz, the thermalization becomes slower than tunneling transfer, and direct photon-assisted current may be observed.

As the radiation-induced electron heating with subsequent thermoelectric/bolometric effects is the main physical reason for photocurrent generation, the correspondence between photocurrent I_{ph} in vertical tunnel structures and electron temperature T_e becomes one-to-one. This correspondence, treated reversely, can be used to measure T_e in highly non-equilibrium conditions, e.g., at strong photoexcitation power. The knowledge of T_e in photoexcited $2d$ materials can shed light on the mechanisms of carrier cooling and provide useful information on the efficiency of light–matter coupling. More precisely, to extract the electron temperature in photoexcited $2d$ material, one may equip it with a vertical tunnel contact and measure I_{ph} at different light intensities. Such a technique can become a convenient alternative to Johnson noise[38] and Coulomb blockade[48] thermometry used previously for similar purposes.

It is worth noting that the magnitude of the photocurrent can be significantly increased with a large area of the tunnel region and a small barrier thickness. The device presented in the article demonstrated a photocurrent of up to 120 pA. And device #2, which has 10 times greater conductivity due to the size of the tunnel junction region, demonstrated 50 times greater photocurrent, up to 5 nA. The sensitivity of device #2 is 0.8 mA W^{-1}. And the noise equivalent power NEP$^* = 830$ pW Hz$^{-1/2}$ (Supplementary Note 2). Using less resistive materials as a barrier layer, for example, WS$_2$[49] will allow for an even more significant increase in sensitivity. Such tunnel micro-detectors demonstrating high photocurrent could be envisioned as a building block for multipixel mid-IR cameras.

Methods

Device fabrication

Devices were made using the dry transfer technique[40]. This involved a standard dry-peel technique to obtain graphene and hBN crystals. The flakes were stacked on top of each other (from top hBN to bottom graphite) using a stamp made of PolyBisphenol carbonate (PC) on poly-dimethylsiloxane (PDMS) and deposited on top of an oxidized (280 nm of SiO$_2$) high-conductivity silicon wafer (KDB-0.001, ~0.001–0.005 Ω cm). The resulting thickness of the hBN layers was measured by atomic force microscopy. Then electron-beam lithography and reactive ion etching with SF6 (30 sccm, 125 W power) were employed to define contact regions in the obtained hBN/graphene/barrier hBN/graphene/hBN/graphite heterostructure. Metal contacts were made by electron-beam evaporating 3 nm of Ti and 70 nm of Au. The second lithography was done to make a cutout to avoid possible shorting of the top and bottom graphene due to the displacement of the thin hBN layer during transfer. It was followed by reactive ion etching using PMMA as the etching mask.

Measurements

The sample was held at 7 K inside a cold finger closed-cycle cryostat (Montana Instruments, s50). I_b–V_b characteristics were measured using Keithley 2636B sourcemeter. Differential conductance was calculated by numerical $I_b(V_b)$ differentiating. $d^2 I_b/dV_b^2$ was measured using AC–DC mixing technique. Source-meter (Keithley Instruments, 2636B) DC voltage and lock-in amplifier (Stanford Research, SR860) output AC sine voltage at 4 Hz frequency was summed up by voltage divider resulting in DC bias with small $V_{AC} = 4.8$ mV (rms) component applied to the sample. Second derivative of I_b–V_b was calculated from lock-in second harmonic readings $I_{2\omega}$ at +90° phase as $d^2 I_b/dV_b^2 = -\sqrt{2}I_{2\omega}/V_{AC}^2$. Photocurrent was also measured using lock-in amplifier. Linearly polarized light from a quantum cascade laser with a wavelength of 8.6 μm was modulated by a chopper at a frequency of 8 Hz. Light was focused by ZnSe lens through polypropylene film cryostat window to an almost diffraction-limited spot. Motorized XY stage allowed precise aligning of sample and laser spot. Binding of the chopper phase was done by comparing the photocurrent phase with that obtained in the case of laser current modulation and additionally controlled from amplified waveforms on the oscilloscope. Deeper details are presented in Supplementary Note 1.

Data availability

The authors declare that the data supporting the findings are available within the paper and its supplementary information. D.A.M. can also provide data upon reasonable request.

References

1. Petric, A. O. et al. Mid-infrared spectral diagnostics of luminous infrared galaxies. *Astrophys. J.* **730**, 28 (2011).
2. Rieke, G. H. et al. The mid-infrared instrument for the James webb space telescope, I: Introduction. *Publ. Astron. Soc. Pac.* **127**, 584 (2015).
3. Ring, F., Jung, A. & Žuber, J. *Infrared Imaging: A Casebook in Clinical Medicine* (IOP Publishing, 2015).
4. Ciampa, F., Mahmoodi, P., Pinto, F. & Meo, M. Recent advances in active infrared thermography for non-destructive testing of aerospace components. *Sensors* **18**, 609 (2018).
5. Popa, D. & Udrea, F. Towards integrated mid-infrared gas sensors. *Sensors* **19**, 2076 (2019).
6. Low, T. et al. Polaritons in layered two-dimensional materials. *Nat. Mater.* **16**, 182–194 (2017).
7. Zheng, Z. et al. Highly confined and tunable hyperbolic phonon polaritons in van der Waals semiconducting transition metal oxides. *Adv. Mater.* **30**, 1705318 (2018).

8. Ma, W. et al. In-plane anisotropic and ultra-low-loss polaritons in a natural van der Waals crystal. *Nature* **562**, 557–562 (2018).

9. Taboada-Gutiérrez, J. et al. Broad spectral tuning of ultra-low-loss polaritons in a van der Waals crystal by intercalation. *Nat. Mater.* **19**, 964–968 (2020).

10. Dai, S. et al. Tunable phonon polaritons in atomically thin van der Waals crystals of boron nitride. *Science* **343**, 1125–1129 (2014).

11. Castilla, S. et al. Plasmonic antenna coupling to hyperbolic phonon-polaritons for sensitive and fast mid-infrared photodetection with graphene. *Nat. Commun.* **11**, 4872 (2020).

12. Duan, J. et al. Active and passive tuning of ultranarrow resonances in polaritonic nanoantennas. *Adv. Mater.* **34**, 2104954 (2022).

13. Massicotte, M. et al. Picosecond photoresponse in van der Waals heterostructures. *Nat. Nanotechnol.* **11**, 42–46 (2016).

14. Gao, Y., Zhou, G., Tsang, H. K. & Shu, C. High-speed van der Waals heterostructure tunneling photodiodes integrated on silicon nitride waveguides. *Optica* **6**, 514–517 (2019).

15. Schneider, H. & Liu, H. C. *Quantum Well Infrared Photodetectors,* Vol. 126 of *Springer Series in Optical Sciences* (Springer, Berlin, Heidelberg, 2006).

16. Ershov, M., Ryzhii, V. & Hamaguchi, C. Contact and distributed effects in quantum well infrared photodetectors. *Appl. Phys. Lett.* **67**, 3147–3149 (1995).

17. Ryzhii, V. et al. Infrared photodetectors based on graphene van der Waals heterostructures. *Infrared Phys. Technol.* **84**, 72–81 (2017).

18. Liu, L., Rahman, S. M., Jiang, Z., Li, W. & Fay, P. Advanced terahertz sensing and imaging systems based on integrated III–V interband tunneling devices. *Proc. IEEE* **105**, 1020–1034 (2017).

19. Gayduchenko, I. et al. Tunnel field-effect transistors for sensitive terahertz detection. *Nat. Commun.* **12**, 543 (2021).

20. Kazarinov, R. & Suris, R. Electric and electromagnetic properties of semiconductors with a superlattice. *Sov. Phys. Semicond.* **6**, 120–131 (1972).

21. Rogalski, A., Martyniuk, P. & Kopytko, M. InAs/GaSb type-II superlattice infrared detectors: future prospect. *Appl. Phys. Rev.* **4**, 031304 (2017).

22. Wei, Y. et al. Uncooled operation of type-II InAs/GaSb superlattice photodiodes in the midwavelength infrared range. *Appl. Phys. Lett.* **86**, 1–3 (2005).

23. Faist, J. et al. Quantum cascade laser. *Science* **264**, 553–556 (1994).

24. Ryzhii, V. et al. Voltage-tunable terahertz and infrared photodetectors based on double-graphene-layer structures. *Appl. Phys. Lett.* **104**, 163505 (2014).

25. Ryzhii, V., Dubinov, A. A., Aleshkin, V. Y., Ryzhii, M. & Otsuji, T. Injection terahertz laser using the resonant inter-layer radiative transitions in double-graphene-layer structure. *Appl. Phys. Lett.* **103**, 10–14 (2013).

26. Massicotte, M. et al. Photo-thermionic effect in vertical graphene heterostructures. *Nat. Commun.* **7**, 12174 (2016).

27. Xie, B. et al. Probing the inelastic electron tunneling via the photocurrent in a vertical graphene van der Waals heterostructure. *ACS Nano* **17**, 18352–18358 (2023).

28. Ma, Q. et al. Tuning ultrafast electron thermalization pathways in a van der Waals heterostructure. *Nat. Phys.* **12**, 455–459 (2016).

29. Kuzmina, A. et al. Resonant light emission from graphene/hexagonal boron nitride/graphene tunnel junctions. *Nano Lett.* **21**, 8332–8339 (2021).

30. Yadav, D. et al. Terahertz wave generation and detection in double-graphene layered van der Waals heterostructures. *2D Mater.* **3**, 045009 (2016).

31. Mishchenko, A. et al. Twist-controlled resonant tunnelling in graphene/boron nitride/graphene heterostructures. *Nat. Nanotechnol.* **9**, 808–813 (2014).

32. Ghazaryan, D. A. et al. Twisted monolayer and bilayer graphene for vertical tunneling transistors. *Appl. Phys. Lett.* **118**, 183106 (2021).

33. Chandni, U., Watanabe, K., Taniguchi, T. & Eisenstein, J. P. Signatures of phonon and defect-assisted tunneling in planar metal-hexagonal boron nitride-graphene junctions. *Nano Lett.* **16**, 7982–7987 (2016).

34. Greenaway, M. T. et al. Tunnel spectroscopy of localised electronic states in hexagonal boron nitride. *Commun. Phys.* **1**, 1–7 (2018).

35. Crossno, J., Liu, X., Ohki, T. A., Kim, P. & Fong, K. C. Development of high frequency and wide bandwidth Johnson noise thermometry. *Appl. Phys. Lett.* **106**, 023121 (2015).

36. Fong, K. C. & Schwab, K. C. Ultrasensitive and wide-bandwidth thermal measurements of graphene at low temperatures. *Phys. Rev. X* **2**, 031006 (2012).

37. Fong, K. C. et al. Measurement of the electronic thermal conductance channels and heat capacity of graphene at low temperature. *Phys. Rev. X* **3**, 041008 (2013).

38. Betz, A. C. et al. Supercollision cooling in undoped graphene. *Nat. Phys.* **9**, 109–112 (2013).

39. Tikhonov, E. S. et al. Noise thermometry applied to thermoelectric measurements in InAs nanowires. *Semicond. Sci. Technol.* **31**, 104001 (2016).

40. Kretinin, A. V. et al. Electronic properties of graphene encapsulated with different two-dimensional atomic crystals. *Nano Lett.* **14**, 3270–3276 (2014).

41. Vdovin, E. et al. Phonon-assisted resonant tunneling of electrons in graphene–boron nitride transistors. *Phys. Rev. Lett.* **116**, 186603 (2016).

42. Fainberg, B. D. Photon-assisted tunneling through molecular conduction junctions with graphene electrodes. *Phys. Rev. B* **88**, 245435 (2013).

43. Platero, G. & Aguado, R. Photon-assisted transport in semiconductor nanostructures. *Phys. Rep.* **395**, 1–157 (2004).

44. Kleinekathöfer, U., Li, G., Welack, S. & Schreiber, M. Switching the current through model molecular wires with Gaussian laser pulses. *Europhys. Lett.* **75**, 139 (2006).

45. Tien, P. & Gordon, J. Multiphoton process observed in the interaction of microwave fields with the tunneling between superconductor films. *Phys. Rev.* **129**, 647 (1963).

46. Li, Q. & Das Sarma, S. Finite temperature inelastic mean free path and quasiparticle lifetime in graphene. *Phys. Rev. B—Condens. Matter Mater. Phys.* **87**, 1–11 (2013).

47. Britnell, L. et al. Electron tunneling through ultrathin boron nitride crystalline barriers. *Nano Lett.* **12**, 1707–1710 (2012).

48. Meschke, M., Kemppinen, A. & Pekola, J. P. Accurate Coulomb blockade thermometry up to 60 kelvin. *Philos. Trans. R. Soc. A: Math. Phys. Eng. Sci.* **374**, 20150052 (2016).

49. Bai, Z. et al. Highly tunable carrier tunneling in vertical graphene–WS2–graphene van der Waals heterostructures. *ACS Nano* **16**, 7880–7889 (2022).

Acknowledgements

Author contributions

Competing interests

The authors declare no competing interests.

Additional information

Supplementary information The online version contains supplementary material available at https://doi.org/10.1038/s41699-024-00470-z.

Correspondence and requests for materials should be addressed to Dmitry A. Mylnikov, Denis A. Bandurin or Dmitry A. Svintsov.

Reprints and permissions information is available at http://www.nature.com/reprints

Publisher's note Springer Nature remains neutral with regard to jurisdictional claims in published maps and institutional affiliations.